Euler Calculations for Flowfield of a Helicopter Rotor in Hover

R. K. Agarwal* and J. E. Deese†
McDonnell Douglas Research Laboratories, St. Louis, Missouri

Aerodynamic loads on a multibladed helicopter rotor in hovering flight are calculated by solving the three-dimensional Euler equations in a rotating coordinate system on body-conforming curvilinear grids around the blades. Euler equations are recast in the absolute flow variables so that the absolute flow in the far field is uniform but the relative flow is nonuniform. Equations are solved for the absolute flow variables employing Jameson's finite-volume explicit Runge-Kutta time-stepping scheme. Rotor-wake effects are modeled in the form of a correction applied to the geometric angle of attack along the blades. This correction is obtained by computing the local induced downwash with a free-wake analysis program. The calculations are performed on a CRAY X/MP-48 for a model helicopter rotor in hover at various collective pitch angles. The results compared with experimental data.

Introduction

As computing power has progressively increased over the past decade, the development of computational codes for the flowfield of a helicopter rotor in hover and forward flight has progressed from the solution of transonic small disturbance equations[1] to full potential equations,[2-6] and more recently to that of Euler equations.[7,8] This paper describes an Euler solver for calculating the inviscid transonic flow on rotor blades in hover or forward flight.

For calculating the inviscid transonic flow about hovering or advancing rotors, Euler equations accurately describe wave drag, shock position, and shock-pressure rise. Euler equations also admit vortical solutions. This feature is especially attractive for helicopter rotor flowfield calculations which are characterized by transonic shocks, complex vortical wakes, and blade-vortex interactions.

To calculate the forces on a hovering or advancing rotor, we need to accurately predict the development of the vortical wake (as shown in Fig. 1). In particular, two features of the wake must be properly determined—first, the contraction of the helical wake as it extends in the axial direction below the rotor, and second, the interaction of the tip vortex of one rotor blade with the following blade. Unlike the nonlinear potential flow equation, Euler equations allow the transport of vorticity, rollup of the wake following the blade, and convection of tip vortex past the blade, thus providing a better model for prediction of aerodynamic loads on hovering and advancing rotors. However, at the present stage of development, there are still limitations associated with finite-difference computations of the Euler equations for predicting the development of vortical wakes. The key problem is false diffusion of vorticity due to truncation error and artificial viscosity in the numerical algorithm employed in the Euler solver. Substantial grid refinement and high-order-accurate differencing may alleviate this problem, but the computational power of the CRAY-2 class of supercomputers will be required.

Presently, the rotor-wake effects are modeled in the form of a correction applied to the geometric angle of attack of the blades. This correction varies along the blade span and reduces the geometric angle of attack by 2–5 deg, depending upon the flow conditions. The correction is the same for all blades in hover flight but there is also an azimuthal variation in forward flight. This correction, for a given rotor and flight condition, is computed with the free-wake analysis programs HOVER and B-TRIM of McDonnell Douglas Helicopter Company for hover and forward flight conditions, respectively.

Both the HOVER and the B-TRIM codes are based on lifting-line theory and provide estimates of the induced downwash v_i and the induced angle of attack α_i. A linear distribution of the vortex lines along the blade span is assumed, except near the tip, where location and strength of the tip vortex are modeled. For the wake, we assume a helical spiral which contracts and expands in response to the local self-induced velocity of the point vortex distribution along the helix. The induced downwash v_i is computed by use of the Biot-Savart law and the local induced angle of attack is computed from the relation $\alpha_i = \tan^{-1}(v_i/\Omega r)$, where Ω is the rotational velocity of the rotor and r is the local radial distance of the blade section from rotor axis. Since α_i has a negative value, the influence of the vortical wake reduces the effective angle of attack.

In this paper, transonic flowfields about a helicopter rotor in hover are calculated by solution of the three-dimensional Euler equations in a rotating coordinate system on body-confirming curvilinear grids around the blades.

A modular solution approach is adopted wherein an independently generated grid is coupled with the flow solver. A three-dimensional grid around the blade is generated as an assembly of two-dimensional spanwise sectional grids. The two-dimensional section O-grids around an airfoil are generated by application of the algebraic grid-generation method of Eiseman. The Euler solver is developed with the finite-volume scheme proposed by Jameson, Schmidt, and Turkel[9]; however, essential modifications are necessary in the formulation of the Euler equations and in implementation of the numerical scheme to accurately solve rotary-wing flowfields. Euler equations are formulated in a rotating coordinate system attached to the rotor blades, but are recast in the absolute-flow variables; thus, the absolute flow in the far field remains uniform but the relative flow is nonuniform and the equations are solved for the absolute-flow variables. This formulation allows more accurate calculation of the fluxes in the finite-volume method and becomes essential for obtaining accurate solutions on nonuniform grids. This ap-

Presented as Paper 86-1782 at the AIAA 4th Applied Aerodynamics Conference, San Diego, CA, June 7–11, 1986; received June 10, 1986; revision received Oct. 24, 1986. Copyright © American Institute of Aeronautics and Astronautics, Inc., 1987. All rights reserved.

*Senior Scientist. Associate Fellow AIAA.
†Scientist. Member AIAA.

proach has previously been used by Holmes and Tong[10] in developing the Euler solver for turbomachinery blade rows.

Calculations are presented for the flowfield of a model helicopter rotor in hover at various collective pitch angles. Comparisons with the experimental data of Caradonna and Tung[11] are presented. Computations were performed on a CRAY X/MP-48.

Governing Equations

Compressible Euler equations are formulated in a Cartesian reference frame rotating with angular velocity Ω of the rotor. The equations are recast in the absolute-flow variables so that the absolute flow in the far field is uniform but the relative flow is nonuniform; we solve for the absolute-flow variables. This formulation allows more accurate calculation of the fluxes in the finite-volume method and becomes essential for obtaining accurate solutions on nonuniform grids.

Let (u,v,w), (u_r,v_r,w_r), and $(u_\Omega,v_\Omega,w_\Omega)$ denote the absolute, relative, and rotational velocity components respectively in the rotating Cartesian coordinate system (x,y,z) shown in Fig. 1. The following relationships hold among the various velocity components:

$$u=u_r-u_\Omega,\quad v=v_r-v_\Omega \text{ and } w=w_r-w_\Omega \tag{1}$$

For a hovering rotor, rotating with a uniform angular velocity Ω about the y axis (as shown in Fig. 1),

$$u_\Omega=-\Omega z, v_\Omega=0 \text{ and } w_\Omega=\Omega x \tag{2}$$

Let p and ρ denote pressure and density, respectively, and E and H define total roenergy and total rothalpy as follows:

$$E=\frac{p}{(\gamma-1)\rho}+\frac{1}{2}(u_r^2+v_r^2+w_r^2)-\frac{1}{2}(u_\Omega^2+w_\Omega^2) \tag{3}$$

$$H=E+\frac{p}{\rho} \tag{4}$$

In a rotating coordinate system attached to the blades (as shown in Fig. 1), the compressible Euler equations can be written as

$$\frac{\partial q}{\partial t}+\frac{\partial L}{\partial x}+\frac{\partial M}{\partial y}+\frac{\partial N}{\partial z}=T \tag{5}$$

where

$$q=\begin{bmatrix}\rho\\ \rho u_r\\ \rho v_r\\ \rho w_r\\ \rho E\end{bmatrix},\quad L=\begin{bmatrix}\rho u_r\\ \rho u_r^2+p\\ \rho u_r v_r\\ \rho u_r w_r\\ \rho u_r H\end{bmatrix},\quad M=\begin{bmatrix}\rho v_r\\ \rho v_r u_r\\ \rho v_r^2+p\\ \rho v_r w_r\\ \rho v_r H\end{bmatrix}$$

$$N=\begin{bmatrix}\rho w_r\\ \rho w_r u_r\\ \rho w_r v_r\\ \rho w_r^2+p\\ \rho w_r H\end{bmatrix},\quad T=\begin{bmatrix}0\\ \rho\Omega^2 x-2\rho\Omega w_r\\ 0\\ \rho\Omega^2 z+2\rho\Omega u_r\\ 0\end{bmatrix}$$

Equation (3) is recast in terms of absolute-velocity components $(u,v,w,)$ using Eq. (1), and the total energy e and total enthalpy h are defined as

$$e=\frac{p}{(\gamma-1)\rho}+\frac{1}{2}(u^2+v^2+w^2)=E-uu_\Omega-ww_\Omega \tag{6}$$

$$h=e+\frac{p}{\rho}=Huu_\Omega-ww_\Omega \tag{7}$$

Equation (5) then becomes

$$\frac{\partial W}{\partial t}+\frac{\partial F_x}{\partial x}+\frac{\partial F_y}{\partial y}+\frac{\partial F_z}{\partial z}+u_\Omega\frac{\partial W}{\partial x}+w_\Omega\frac{\partial W}{\partial x}=G \tag{8}$$

where

$$W=\begin{bmatrix}\rho\\ \rho u\\ \rho v\\ \rho w\\ \rho e\end{bmatrix},\quad F_x=\begin{bmatrix}\rho u\\ \rho u^2+p\\ \rho uv\\ \rho uw\\ \rho uh\end{bmatrix},\quad F_y=\begin{bmatrix}\rho v\\ \rho vu\\ \rho v^2+p\\ \rho vw\\ \rho vh\end{bmatrix}$$

$$F_z=\begin{bmatrix}\rho w\\ \rho wu\\ \rho wv\\ \rho w^2+p\\ \rho wh\end{bmatrix},\quad G=\begin{bmatrix}0\\ -\rho\Omega w\\ 0\\ \rho\Omega u\\ 0\end{bmatrix}$$

Let $F=F_x\hat{e}_x+F_y\hat{e}_y+F_z\hat{e}_z$, and $u_\Omega=u_\Omega\hat{e}_x+v_\Omega\hat{e}_y+w_\Omega\hat{e}_z$, where $(\hat{e}_x,\hat{e}_y,\hat{e}_z)$ are the unit vectors in the (x,y,z) coordinate system. Then Eq. (8) can be written as

$$\frac{\partial W}{\partial t}+\nabla\cdot F+u_\Omega\cdot\nabla W=G \tag{9}$$

We solve Eq. (9) using the finite-volume method described in the next section.

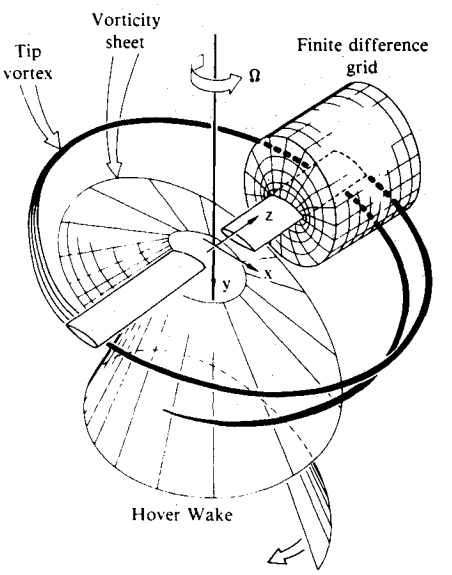

Fig. 1 Schematic of a two-bladed, helicopter rotor wake with an embedded finite-difference grid and the coordinate system (after Strawn and Caradonna).

Finite-Volume Method

To apply the finite-volume method, Eq. (9) is written in the integral form

$$\frac{\partial}{\partial t}\iiint_V W\,dV+\iint_{\partial S}\hat{n}\cdot F\,ds+\iint_{\partial S}u_\Omega\cdot\hat{n}W\,ds=\iiint_V G\,dV \quad (10)$$

for a domain V with a bounding surface ∂S, where $\hat{n}$ denotes the unit outward normal vector to the surface element ds.

Substituting for u_Ω in Eq. (10), we obtain

$$\frac{\partial}{\partial t}\iiint_V W\,dV+\iint_{\partial S}\hat{n}\cdot F\,ds-\Omega\iint_{\partial S}zW(\hat{e}_x\cdot\hat{n})\,ds$$
$$+\Omega\iint_{\partial S}xW(\hat{e}_z\cdot\hat{n})\,ds=\iiint_V G\,dV \quad (11)$$

The computational domain is divided into hexahedral cells denoted by the subscripts (i,j,k) as shown in Fig. 2. Assuming that the dependent variables are known at the center of each cell, we obtain a system of ordinary differential equations by applying Eq. (11) separately to each cell. These equations have the form

$$\frac{d}{dt}(J_{ijk}W_{ijk})+P_{ijk}+Q_{ijk}+R_{ijk}=J_{ijk}G_{ijk} \quad (12)$$

where J_{ijk} is the cell volume, P_{ijk} represents the net absolute flux out of the cell, and Q_{ijk} and R_{ijk} are rotational fluxes out of the cell. The calculation of J_{ijk}, P_{ijk}, Q_{ijk}, and R_{ijk} for a hexahedral cell, shown in Fig. 2b, is described in Appendix A. We rewrite Eq. (12) as

$$\frac{d}{dt}(J_{ijk}W_{ijk})+\mathfrak{F}_{ijk}=0 \quad (13)$$

The finite-volume scheme [Eq. (13)] constructed in this manner reduces to a central-difference scheme on a Cartesian mesh and is second-order accurate, provided that the mesh is sufficiently smooth and without any abrupt changes in cell shape and volume. The scheme [Eq. (13)] is not dissipative, and therefore allows undamped oscillations at odd and even mesh points.

To suppress the tendency for odd- and even-point decoupling and to prevent the appearance of oscillations in regions containing severe pressure gradients near shock waves and stagnation points, the finite-volume scheme is augmented by the addition of artificial dissipative terms. Equation (13) is replaced by

$$\frac{d}{dt}(J_{ijk}W_{ijk})+\mathfrak{F}_{ijk}-D_{ijk}=0 \quad (14)$$

where D_{ijk} denotes the dissipative terms which are generated by dissipative fluxes. Jameson[9] has established that an effective form of dissipative terms for flows with discontinuities is a blend of second and fourth differences with coefficients that depend on the local pressure gradient. Dissipative terms are constructed as follows:

$$D_{ijk}=(D_x+D_y+D_z)W_{ijk} \quad (15)$$

where

$$D_xW_{ijk}=d_{i+\frac{1}{2},j,k}-d_{i-\frac{1}{2},j,k} \quad (16)$$

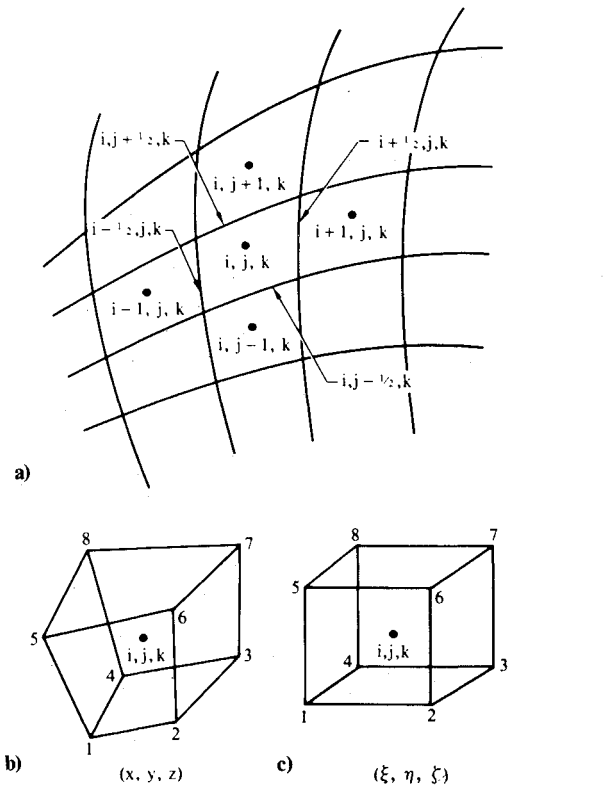

Fig. 2 a) Division of the computational domain into hexahedral cells (sketched on the k surface), b) a hexhedral cell in the physical domain, and c) the corresponding unit cube in the computational domain.

The dissipative flux $d_{i+\frac{1}{2},j,k}$ is defined as

$$d_{i+\frac{1}{2},j,k}=\frac{J_{i+\frac{1}{2},j,k}}{(\Delta t_l)_{i+\frac{1}{2},j,k}}$$
$$\times[\epsilon^{(2)}_{i+\frac{1}{2},j,k}\Delta_xW_{ijk}-\epsilon^{(4)}_{i+\frac{1}{2},j,k}\Delta_x^3W_{i,-1,j,k}] \quad (17)$$

where Δ_x denotes the forward difference operator $\Delta_x=(W_{i,+1,j,k}-W_{i,j,k})$, and $\epsilon^{(2)}$ and $\epsilon^{(4)}$ are adaptive coefficients defined below. We define

$$\nu_{ijk}=\left|\frac{p_{i+1,j,k}-2p_{ijk}+p_{i-1,j,k}}{p_{i+1,j,k}+2p_{ijk}+p_{i-1,j,k}}\right| \quad (18)$$

$$\epsilon^{(2)}_{i+\frac{1}{2},j,k}=\kappa^{(2)}\max(\nu_{i+1,j,k},\nu_{ijk}) \quad (19)$$

and

$$\epsilon^{(4)}_{i+\frac{1}{2},j,k}=\max[0,(\kappa^{(4)}-\epsilon^{(2)}_{i+\frac{1}{2},j,k})] \quad (20)$$

where typical values of the constants $\kappa^{(2)}$ and $\kappa^{(4)}$ are $\kappa^{(2)}=1$, $\kappa^{(4)}=1/32$. $(\Delta t_l)_{ijk}$ is defined in Appendix B. The terms D_yW_{ijk} and D_zW_{ijk} in Eq. (15) are calculated in an analogous manner.

The scaling $J/\Delta t$ in Eq. (17) conforms to the inclusion of the cell volume in the dependent variables of Eq. (14). Since Eq. (17) contains undivided differences, it follows that if $\epsilon^{(2)}=0(\Delta x^2)$ and $\epsilon^{(4)}=0(1)$, then the added terms are of $0(\Delta x^3)$, as will be the case in the regions where the flow is smooth. Near a shock wave $\epsilon^{(2)}=0(1)$, and the scheme behaves locally as a first-order-accurate scheme.

Time-Stepping Scheme

The classical fourth-order Runge-Kutta scheme is used to integrate Eq. (14). Suppressing the subscripts (i,j,k), we can write Eq. (14) as

$$\frac{dW}{dt}+\frac{1}{J}[\mathfrak{F}(W)-D(W)]=0 \tag{21}$$

At time level n, we set

$$W^{(0)}=W^n$$

$$W^{(1)}=W^{(0)}-\frac{\Delta t}{8J}[\mathfrak{F}W^{(0)}-DW^{(0)}]$$

$$W^{(2)}=W^{(0)}-\frac{\Delta t}{6J}[\mathfrak{F}W^{(1)}-DW^{(0)}]$$

$$W^{(3)}=W^{(0)}-\frac{\Delta t}{4J}[\mathfrak{F}W^{(2)}-DW^{(0)}]$$

$$W^{(4)}=W^{(0)}-\frac{\Delta t}{2J}[\mathfrak{F}W^{(3)}-DW^{(0)}]$$

$$W^{n+1}=W^{(4)} \tag{22}$$

In Eq. (22), the dissipative terms are frozen at their values in the first stage, thus avoiding expensive computations for each stage. The scheme is fourth-order accurate in time, and is stable for Courant numbers $\leq 2\sqrt{2}$. The scheme has the property that if $[\mathfrak{F}W^n-DW^n]=0$, then $W^{(1)}=W^{(0)}$, $W^{n+1}=W^n$, and the steady-state solution is $\mathfrak{F}W^n-DW^n=0$, independent of time step Δt. Thus, a variable time-step (Δt_ℓ) determined by the bound on the local Courant number can be used to accelerate convergence to steady state without altering the steady state. To obtain time-accurate calculations of unsteady flow phenomena, we determine the allowable time step by the minimum value of the Courant number in the field.

Boundary Conditions

Special considerations are required to determine the fluxes in Eq. (13) at the boundaries. Far-field boundary conditions are applied at a finite distance from the blade surface, while flow tangency is applied at the blade surface. In addition, a periodic condition is applied in the plane containing the blade root for the hover case. A number of other boundary conditions are also explored for the plane containing the blade root.

At the solid boundary, flow tangency implies zero convected fluxes across the boundary; the only contribution to flux balance in Eq. (13) comes from the pressure. The normal pressure gradient at the blade surface is estimated from the condition that $\partial(\rho V_n)/\partial t=0$, where V_n is the normal velocity component. The pressure at the wall is then calculated from the pressure at the adjacent cell centers with the known value of $\partial p/\partial n$.

The treatment of the far-field boundary condition is based on the introduction of Riemann invariants for a one-dimensional flow normal to the boundary.[12] Let subscripts ∞ and e denote far-field values and values extrapolated from the interior cells adjacent to the boundary, and let V_n and a be the velocity component normal to the boundary and the speed of sound, respectively.

If the flow in the far field is subsonic, we introduce fixed and extrapolated Riemann invariants

$$R_\infty=V_{n\infty}-\frac{2a_\infty}{\gamma-1} \text{ and } R_e=V_{ne}+\frac{2a_e}{\gamma-1}$$

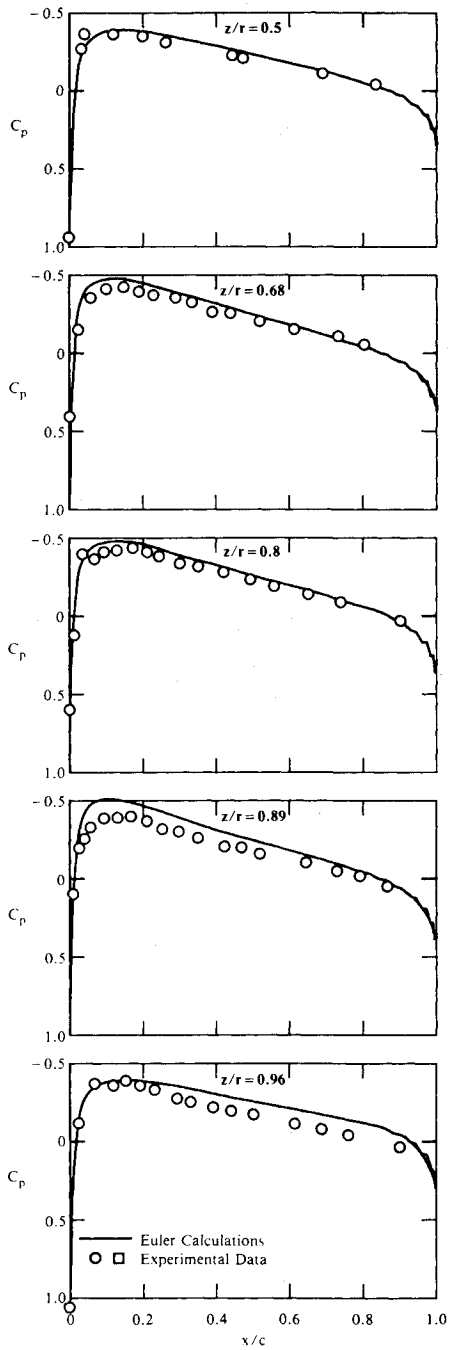

Fig. 3 Surface pressure distribution on a nonlifting rotor in hover; $M_t=0.52$, $\theta_c=0$ deg, $\mathcal{A}R=6.0$, untwisted, untapered, NACA-0012 blade, $97\times33\times21$ mesh.

corresponding to incoming and outgoing waves. These invariants may be added and subtracted to obtain

$$V_n=\tfrac{1}{2}(R_e+R_\infty) \text{ and } a=\tfrac{1}{4}(\gamma-1)(R_e-R_\infty)$$

where V_n and a are the actual normal velocity component and the speed of sound to be specified in the far field, respectively. At an outflow boundary, the tangential velocity component and entropy are extrapolated from the interior, while at an inflow boundary they are specified as having far-field values. These four quantities provide a complete definition of the flow in the far field.

If the flow is supersonic in the far field, all the quantities are specified at the inflow boundary, and they are all extrapolated from the interior at an outflow boundary.

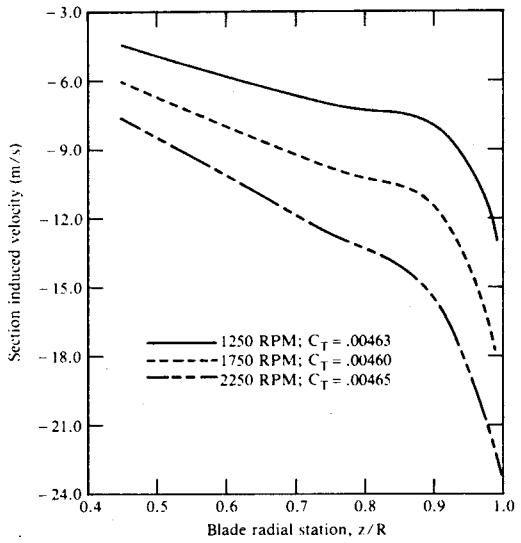

Fig. 4 Radial-induced velocity distributions on a two-bladed hovering rotor obtained with the Free-Wake Analysis Program HOVER of McDonnell Douglas Helicopter Company; untwisted, untapered, NACA-0012 blade, $AR=6.0$, $\theta_c=8$ deg, $R=1.143$ m, $C=0.1905$ m.

In the plane containing the blade root, two kinds of boundary conditions, 1) periodic and 2) $\partial W/\partial z=0$, were implemented; condition 2) yielded better results. Alternative boundary conditions for this plane are presently under investigation.

Computed Examples

Computations are performed for the flowfield of a model helicopter rotor in hover at various collective pitch angles. The rotor has two blades of aspect ratio equal to 6 which are untwisted, untapered, and have the NACA-0012 airfoil section. The experiments on this rotor have been performed by Caradonna and Tung[16] at NASA Ames Research Center for a range of blade tip Mach numbers M_t and collective pitch angles θ_c. Computations are performed on a $97\times33\times21$ mesh on a CRAY X/MP-48. A typical computation requires 2 million words of main memory and $2.1\cdot10^{-5}$ s of CPU time per mesh point for each iteration. The fully vectorized version of the code decreases CPU time by a factor of 3 and the microtasked version of the code on four processors of the CRAY X/MP-48 provides an additional time gain factor of approximately 3.7 in wall clock time.

A six-order-of-magnitude reduction in the residual for density was obtained in approximately 800 time steps at a Courant number of 2 and the solution was considered fully converged. A converged solution required approximately 19 min of CPU time on CRAY X/MP-48. The residual for density is defined as the root-mean-square value of $\partial\rho/\partial t$ (calculated as $\Delta\rho/\Delta t$ for the complete time step).

Nonlifting Case: $M_t=0.44$, $\theta_c=0$

Figure 3 shows the surface pressure distribution on the nonlifting blade at different spanwise locations. The agreement between the Euler calculations and the experimental data is excellent.

Lifting Cases: $M_t=0.57$, $\theta_c=8$ deg,

$M_t=0.877$, $\theta_c=8$ deg

As mentioned before in the introduction, for these calculations the rotor-wake effects are modeled in the form of a

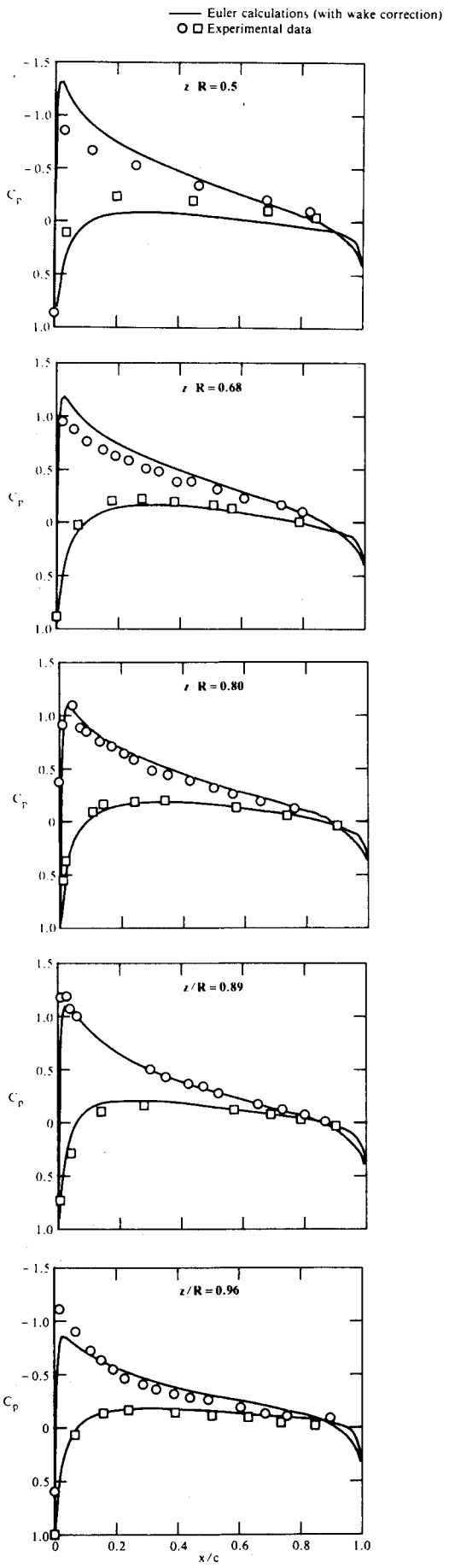

Fig. 5 Surface pressure distributions on a lifting rotor in hover; $M_t=0.44$, $\theta_c=8$ deg, $AR=6.0$, untwisted, untapered, NACA-0012 blade, $97\times33\times21$ mesh.

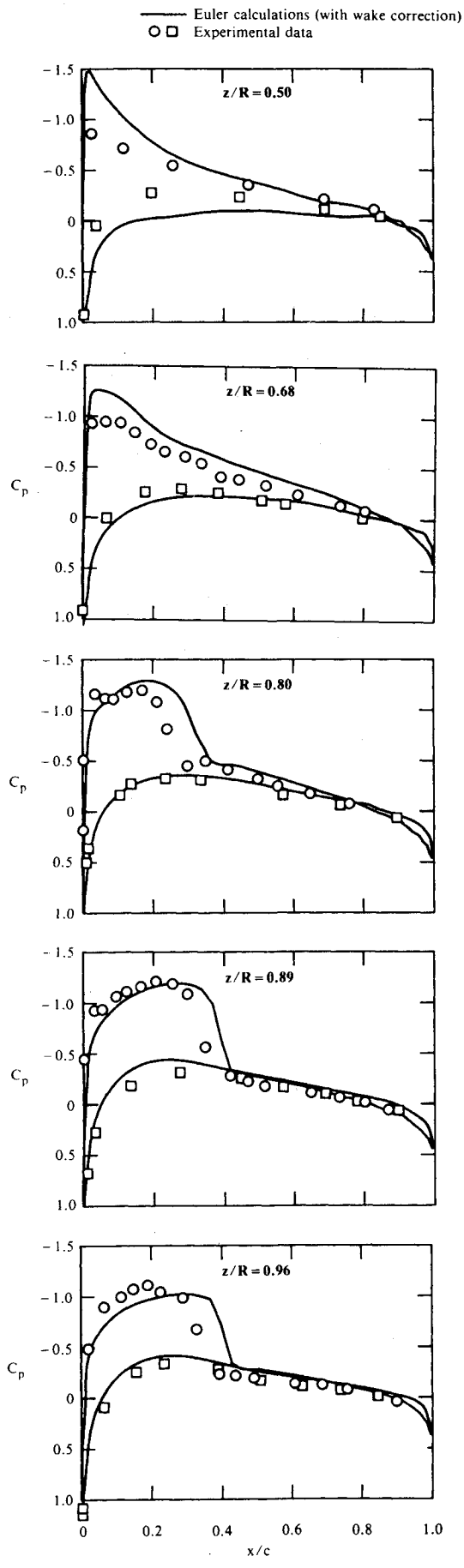

Fig. 6 Surface pressure distributions on a lifting rotor in hover; $M_t = 0.877$, $\theta_c = 8$ deg, $\mathcal{A}R = 6.0$, untwisted, untapered, NACA-0012 blade, 97×33×21 mesh.

correction applied to the geometric angle of attack of the blades. The free-wake analysis program HOVER of McDonnell Douglas Helicopter Company is used to calculate the induced downwash v_i. The results of these calculations are shown in Fig. 4. The induced angle of attack is calculated from the relation $\alpha_i = \tan^{-1}(v_i/\Omega r)$, where Ω is the rotational velocity of the rotor and r is the local radial distance of the blade section from the rotor axis. As can be seen from Fig. 4, the slope of the curve v_i as a function of r remains constant except near the blade tip. For 95% of the blade span, α_i can be taken as approximately 3.8 deg for both cases a) and b). The effective angle of attack thus becomes $\alpha_e = \theta_c - \alpha_i = 4.2$ deg. Figures 5 and 6 show the surface-pressure distribution on the blade at various spanwise stations for cases 1) and 2), respectively. The agreement between the calculations and the experimental data is satisfactory. Perhaps better modeling of the wake effects will improve the results of the calculation. Further investigation is also needed to formulate proper boundary conditions in the x-y plane at blade root.

Conclusions

A three-dimensional Euler solver has been developed for calculating the transonic flow on rotor blades of a helicopter in hover. The computational code is robust, efficient, and accurate. With the computing power currently available on the CRAY X/MP or CYBER 205 class of machines, wake modeling is still needed for accurate calculation of aerodynamic loads. Extensive grid refinement and a large computational domain are needed to capture the vortical wake, requiring use of the CRAY 2 class of machines. A realistic approach appears to be the integration of a free-wake analysis program with the Euler solver.

Appendix A: Calculation of J_{ijk}, P_{ijk}, a_{ijk}, and R_{ijk} in Eq. (12)

For a hexahedral cell shown in Fig. 2b, the cell volume J_{ijk} is computed as

$$J_{ijk} = T_{1236} + T_{3867} + T_{1685} + T_{1348} + T_{3816} \tag{A1}$$

where T denotes the volumes of the five tetrahedra.

The integer subscripts on T_{1236} refer to the four vertices of the cell that define the tetrahedron. The volume of the tetrahedron T_{1236} is given by

$$T_{1236} = \begin{bmatrix} x_1 & y_1 & z_1 & 1 \\ x_2 & y_2 & z_2 & 1 \\ x_3 & y_3 & z_3 & 1 \\ x_6 & y_6 & z_6 & 1 \end{bmatrix} \tag{A2}$$

Relations similar to Eq. (A2) can be written for the volumes of other tetrahedra in Eq. (A1).

From Eq. (11),

$$P_{ijk} = \left[\iint_{\partial S} \hat{n} \cdot F \, dS \right]_{ijk} \tag{A3}$$

For the cell shown in Fig. 2b, (A3) takes the form

$$\begin{aligned} P_{ijk} = {} & [(F \cdot S)_{i+\frac{1}{2},j,k} - (F \cdot S)_{i-\frac{1}{2},j,k}] \\ & + [(F \cdot S)_{i,j+\frac{1}{2},k} - (F \cdot S)_{i,j-\frac{1}{2},k}] \\ & + [(F \cdot S)_{i,j,k+\frac{1}{2}} - (F \cdot S)_{i,j,k-\frac{1}{2}}] \end{aligned} \tag{A4}$$

In Eq. (A4), $S_{i+\frac{1}{2},j,k}$ denotes the area of the cell face located at $(i+\frac{1}{2},j,k)$, etc. Again referring to Fig. 2b, the area of a

cell face 1234, for example, can be obtained as

$$S_{1234} = (S_x)_{1234}\hat{e}_x + (S_y)_{1234}\hat{e}_y + (S_z)_{1234}\hat{e}_z$$

where

$$(S_x)_{1234} = \tfrac{1}{2}[(y_2 - y_4)(z_3 - z_1) - (z_2 - z_4)(y_3 - y_1)]$$

$$(S_y)_{1234} = \tfrac{1}{2}[(z_2 - z_4)(x_3 - x_1) - (x_2 - x_4)(z_3 - z_1)]$$

$$(S_z)_{1234} = \tfrac{1}{2}[(x_2 - x_4)(y_3 - y_1) - (y_2 - y_4)(x_3 - x_1)] \quad \text{(A5)}$$

We can also write

$$S_{1234} = |S_{1234}|\,\hat{n}_{1234}$$

where

$$|S_{1234}| = \sqrt{(S_x)^2_{1234} + (S_y)^2_{1234} + (S_z)^2_{1234}}$$

and $\hat{n}_{1234}$ is the unit outward normal to surface 1234. In Eq. (A4), the quantities on the right side can be expressed as

$$(F\cdot S)_{i+\frac{1}{2},j,k} = [(F_x)_{i+\frac{1}{2},j,k}(S_x)_{i+\frac{1}{2},j,k} + (F_y)_{i+\frac{1}{2},j,k}(S_y)_{i+\frac{1}{2},j,k} + (F_z)_{i+\frac{1}{2},j,k}(S_z)_{i+\frac{1}{2},j,k}] \quad \text{(A6)}$$

In Eq. (A6), S_x, S_y, S_z are given by formulas of the type given in Eq. (A5), and F_x, F_y, F_z are given by Eq. (8) in terms of the variables ρ, ρu, ρv, ρw, p, and ρe which are computed at $(i+\frac{1}{2},j,k)$ by formulas of the type $\rho_{i+\frac{1}{2},j,k} = \frac{1}{2}(\rho_{i,j,k} + \rho_{i+1,j,k})$. In this manner, a complete description of P_{ijk} is obtained.

Q_{ijk} is given by

$$Q_{ijk} = \left[-\Omega\int_\partial\int_S zW(\hat{e}_x\cdot\hat{n})\,ds\right]_{ijk} = \left[-\Omega\int_\partial\int_S zW\,ds_x\right]_{i,j,k}$$

$$= -\Omega[W_{i+\frac{1}{2},j,k}I_{i+\frac{1}{2},j,k} - W_{i-\frac{1}{2},j,k}I_{i-\frac{1}{2},j,k} \quad \text{(A7)}$$

$$+ W_{i,j+\frac{1}{2},k}I_{i,j+\frac{1}{2},k} - W_{i,j-\frac{1}{2},k}I_{i,j-\frac{1}{2},k}]$$

$$+ W_{i,j,k+\frac{1}{2}}I_{i,j,k+\frac{1}{2}} - W_{i,j,k-\frac{1}{2}}I_{i,j,k-1/2} \quad \text{(A8)}$$

where

$$I = \int_{\partial S}\int zds_x \quad \text{(A9)}$$

Referring to Fig. 2b, for the surface 1234,

$$I_{1234}(\text{same as } I_{i,j,k-\frac{1}{2}})$$

$$= 1/6\{(z_1+z_2)(z_2y_1 - z_1y_2) + (z_z+z_3)(z_3y_2 - z_2y_3)$$

$$+ (z_3+z_4)(z_4y_3 - z_3y_4) + (z_4+z_1)(z_1y_4 - z_4y_1)\} \quad \text{(A10)}$$

R_{ijk} is given by

$$R_{ijk} = \left[\Omega\int_{\partial S}\int xW(\hat{e}_z\cdot\hat{n})\,ds\right]_{ijk} = \left[\Omega\int_{\partial S}\int xW\,ds_z\right]_{i,j,k}$$

$$= \Omega[W_{i+\frac{1}{2},j,k}\hat{I}_{i+\frac{1}{2},j,k} - W_{i-\frac{1}{2},j,k}\hat{I}_{i-\frac{1}{2},j,k} \quad \text{(A11)}$$

$$+ W_{i,j+\frac{1}{2},k}\hat{I}_{i,j+\frac{1}{2},k} - W_{i,j-\frac{1}{2},k}\hat{I}_{i,j-\frac{1}{2},k}$$

$$+ W_{i,j,k+\frac{1}{2}}\hat{I}_{i,j,k+\frac{1}{2}} - W_{i,j,k-\frac{1}{2}}\hat{I}_{i,j,k-\frac{1}{2}}] \quad \text{(A12)}$$

where

$$\hat{I} = \int_{\partial S}\int xds_z \quad \text{(A13)}$$

Again, referring to Fig. 2b, for the surface 1234

$$\hat{I}_{1234}\ (\text{same as } \hat{I}_{i,j,k-\frac{1}{2}})$$

$$= 1/6\{(x_1+x_2)(x_1y_2 - x_2y_1) + (x_2+x_3)(x_2y_3 - x_3y_2)$$

$$+ (x_3+x_4)(x_3y_4 - x_4y_3) + (x_4+x_1)(y_1x_4 - x_1y_4)\} \quad \text{(A14)}$$

Appendix B: Calculation of $(\Delta t_\ell)_{i,j,k}$ in Eq. (17)

At a cell point (i,j,k), $(\Delta t_\ell)_{ijk}$ is defined as[13]

$$(\Delta t_\ell)_{i,j,k} = [(\Delta t_x)_{i,j,k}(\Delta t_y)_{i,j,k}(\Delta t_z)_{i,j,k}]/(\Delta t_x)_{i,j,k}(\Delta t_y)_{i,j,k} + (\Delta t_y)_{i,j,k}(\Delta t_z)_{i,j,k} + (\Delta t_z)_{i,j,k}(\Delta t_x)_{i,j,k} \quad \text{(B1)}$$

where

$$(\Delta t_x)_{i,j,k} = \frac{J_{ijk}}{|Q_x| + a\sqrt{[\bar{S}_x]_i^2 + [\bar{S}_y]_i^2 + [\bar{S}_z]_i^2}} \quad \text{(B2)}$$

$$[\bar{S}_x]_i = \tfrac{1}{2}[(S_x)_{i+\frac{1}{2},j,k} + (S_x)_{i-\frac{1}{2},j,k}]$$

$$[\bar{S}_y]_i = \tfrac{1}{2}[(S_y)_{i+\frac{1}{2},j,k} + (S_y)_{i-\frac{1}{2},j,k}]$$

$$[\bar{S}_z]_i = \tfrac{1}{2}[(S_z)_{i+\frac{1}{2},j,k} + (S_z)_{i-\frac{1}{2},j,k}] \quad \text{(B3)}$$

$$Q_x = \{(\rho u_r)_{ijk}[\bar{S}_x]_i + (\rho v_r)_{ijk}[\bar{S}_y]_i + (\rho w_r)_{ijk}[\bar{S}_z]_i\}/\rho_{ijk} \quad \text{(B4)}$$

and a = speed of sound.

Equations analogous to (B2) can be written for $(\Delta t_y)_{ijk}$ and $(\Delta t_z)_{ijk}$. In Eqs. (B3), the $(S_x)_{i+\frac{1}{2},j,k}$ and similar terms are evaluated using formulas analogous to Eqs. (A5). For obtaining a time-accurate solution, the time step at each step of iteration is given by

$$\Delta t \le \min_{i,j,k}\ (\Delta t_\ell) \quad \text{(B5)}$$

Acknowledgments

The authors gratefully acknowledge the assistance of M. Uram of McDonnell Douglas Aerospace Information Services Company with programming on CRAY X/MP-48. The authors would also like to thank D. S. JanakiRam of McDonnell Douglas Helicopter Company for providing the results shown in Fig. 4.

This work was performed under the McDonnell Douglas Independent Research and Development Program.

References

[1]Caradonna, F. X. and Isom, M. P., "Subsonic and Transonic Potential Flow over Helicopter Blades," *AIAA Journal*, Vol. 10, 1972, pp. 1606–1612.

[2]Arieli, R. and Tauber, M. E., "Computation of Subsonic and Transonic Flow about Lifting Rotor Blades," AIAA Paper 79-1667, 1979.

[3]Strawn, R. C. and Caradonna, F. X., "Numerical Modeling of Rotor Flows with a Conservative Form of the Full-Potential Equation," AIAA Paper 86-0079, 1986.

[4]Egolf, T. A. and Sparks, S. P., "Hover Rotor Airload Predictions Using a Full Potential Flow Analysis with a Realistic Wake Geometry," *Proceedings of the 41st Annual Forum of the American Helicopter Society*, 1985.

[5]Egolf, T. A. and Spark, S. P., "A Full Potential Rotor Analysis with Wake Influence Using an Inner-Outer Domain Technique," *Proceedings of the 42nd Annual Forum of the American Helicopter Society,* 1986.

[6]Sankar, L. N. and Prichard, D., "Solution of Transonic Flow Past Rotor Blades Using the Conservative Full Potential Equation," AIAA Paper 85-5012, 1985.

[7]Roberts, T. W. and Murman, E. M., "Solution Method for a Hovering Helicopter Using the Euler Equations," AIAA Paper 85-0436, 1985.

[8]Sankar, L. N., Wake, B. E., and Lekoudis, S. G., "Solution of the Unsteady Euler Equations for Fixed and Rotary Wing Configurations," AIAA Paper 85-0120, 1985.

[9]Jameson, A., Schmidt, W., and Turkel, E., "Numerical Solution of the Euler Equations by Finite Volume Methods Using Runge-Kutta Time-Stepping Schemes," AIAA Paper 81-1259, 1981.

[10]Holmes, D. G. and Tong, S. S., "A Three-Dimensional Euler Solver for Turbomachinery Blade Rows," *Journal of Engineering for Gas Turbines and Power, Transactions of ASME,* Vol. 107, 1985, pp. 258-264.

[11]Cardonna, F. X. and Tung, C., "Experimental and Analytical Studies of a Model Helicopter Rotor in Hover," *Vertica,* Vol. 5, 1981, pp. 149-161.

[12]Jameson, A. and Baker, T. J., "Solution of Euler Equations for Complex Configurations," AIAA Paper 83-1929, 1983.

[13]Agarwal, R. K. and Deese, J. E., "Transonic Wing-Body Calculations Using Euler Equations," AIAA Paper 83-0501, 1983.

From the AIAA Progress in Astronautics and Aeronautics Series . . .

VISCOUS FLOW DRAG REDUCTION—v. 72

Edited by Gary R. Hough, Vought Advanced Technology Center

One of the most important goals of modern fluid dynamics is the achievement of high speed flight with the least possible expenditure of fuel. Under today's conditions of high fuel costs, the emphasis on energy conservation and on fuel economy has become especially important in civil air transportation. An important path toward these goals lies in the direction of drag reduction, the theme of this book. Historically, the reduction of drag has been achieved by means of better understanding and better control of the boundary layer, including the separation region and the wake of the body. In recent years it has become apparent that, together with the fluid-mechanical approach, it is important to understand the physics of fluids at the smallest dimensions, in fact, at the molecular level. More and more, physicists are joining with fluid dynamicists in the quest for understanding of such phenomena as the origins of turbulence and the nature of fluid-surface interaction. In the field of underwater motion, this has led to extensive study of the role of high molecular weight additives in reducing skin friction and in controlling boundary layer transition, with beneficial effects on the drag of submerged bodies. This entire range of topics is covered by the papers in this volume, offering the aerodynamicist and the hydrodynamicist new basic knowledge of the phenomena to be mastered in order to reduce the drag of a vehicle.

Published in 1980,456 pp., 6×9, illus., $35.00 Mem., $65.00 List

TO ORDER WRITE: Publications Order Dept., AIAA, 1633 Broadway, New York, N.Y. 10019